

# Mapping Physical Conditions in Neighboring Hot Cores: NOEMA Studies of W3(H<sub>2</sub>O) and W3(OH)

MORGAN M. GIESE,<sup>1</sup> WILL E. THOMPSON,<sup>2</sup> DARIUSZ C. LIS,<sup>3</sup> AND SUSANNA L. WIDICUS WEAVER<sup>1,2</sup>

<sup>1</sup>*Department of Astronomy, University of Wisconsin-Madison  
475 N Charter St, Madison, Wisconsin 53706, USA*

<sup>2</sup>*Department of Chemistry, University of Wisconsin-Madison  
1101 University Ave, Madison, Wisconsin 53706, USA*

<sup>3</sup>*Jet Propulsion Laboratory, California Institute of Technology  
4800 Oak Grove Drive, Pasadena, CA, 91109, USA*

## ABSTRACT

The complex chemistry that occurs in star-forming regions can provide insight into the formation of prebiotic molecules at various evolutionary stages of star formation. To study this process, we present millimeter-wave interferometric observations of the neighboring hot cores W3(H<sub>2</sub>O) and W3(OH) carried out using the NOEMA interferometer. We have analyzed distributions of six molecules that account for most observed lines across both cores and have constructed physical parameter maps for rotational temperature, column density, and velocity field with corresponding uncertainties. We discuss the derived spatial distributions of these parameters in the context of the physical structure of the source. We propose the use of HCOOCH<sub>3</sub> as a new temperature tracer in W3(H<sub>2</sub>O) and W3(OH) in addition to the more commonly used CH<sub>3</sub>CN. By analyzing the physically-derived parameters for each molecule across both W3(H<sub>2</sub>O) and W3(OH), the work presented herein further demonstrates the impact of physical environment on hot cores at different evolutionary stages.

*Keywords:* Astrochemistry (75) — Star-forming regions (1565) — Interferometry (808) — HII regions (694)

## 1. INTRODUCTION

Complex chemistry occurs at every stage in the star formation process, but significant enhancement of complexity occurs after the collapse of a molecular cloud (Blake & van Dishoeck 1998; van Dishoeck 2006; Herbst & van Dishoeck 2009). In this phase, the icy mantles of dust grains undergo radiative processing via cosmic rays and ultraviolet radiation to form complex organics and other prebiotic molecules (Munoz Caro et al. 2002; Öberg et al. 2011; Altwegg et al. 2019). These prebiotic molecules are commonly studied in star-forming regions and comets, as many of these molecules make up a large majority of the chemical inventory in protoplanetary disks and are crucial in the development of planetary systems (Blake & van Dishoeck 1998; Jørgensen et al. 2012; Widicus Weaver & Friedel 2012; Altwegg et al. 2019; Rivilla et al. 2020; Ligterink et al. 2022). While it is unclear as to how these molecules survive and are delivered to early-stage planets, they could possibly be brought to the system via meteorites and cometary impacts (Oró 1961; Chyba et al. 1990; Chyba & Sagan 1992; Blake & van Dishoeck 1998; van Dishoeck 2006;

Hartogh et al. 2011). Rotational transitions of prebiotic molecules are further useful for studying different stages of star formation as they can provide important information on physical characteristics such as temperatures and densities (Tychoniec et al. 2021). In order to probe these regions, the use of millimeter-wave interferometers has been instrumental in identifying how the physical environment of an interstellar region affects the chemistry that occurs (Jørgensen et al. 2004; Tobin et al. 2011; Tychoniec et al. 2021).

The neighboring hot cores W3(H<sub>2</sub>O) and W3(OH) provide a unique environment to study how the molecular complexity can differ across different sources. The two cores are at different stages of stellar evolution, with W3(OH) being an ultra-compact HII region (Helmich & van Dishoeck 1997; Rivera-Ingraham et al. 2013; Qin et al. 2015; Widicus Weaver et al. 2017; Thompson et al. 2023). Given that they formed from the same parent cloud, these two cores are well-suited for studying how prebiotic chemistry evolves during the star formation process. Both cores exhibit similar, yet distinct, molecular compositions, likely due to their difference in ages.

W3(H<sub>2</sub>O) and W3(OH) are such-named due to the presence of H<sub>2</sub>O and OH masers, respectively, and are at a distance of  $\sim 2$  kpc from Earth with a  $v_{lsr}$  of  $-47$  km s<sup>-1</sup> (Wynn-Williams et al. 1972; Wyrowski et al. 1997; Wilner et al. 1999; Rivera-Ingraham et al. 2013).

Thompson et al. (2023) recently presented results from millimeter-wave interferometric observations of these two cores. Building on this work, herein we present further chemical analysis of the six molecules that were quantitatively analyzed in Thompson et al. (2023). This current study includes detailed parameter maps for these molecules in the two cores based on rotational temperature, column density, and velocity shift relative to  $v_{lsr}$ . Parameter maps show a visualization of the physical conditions within the region, allowing for a deeper insight into the effects of star formation on prebiotic molecules in hot cores.

## 2. OBSERVATIONS AND DATA REDUCTION

While specific details on the observations and data reduction process are described in Thompson et al. (2023), an overview of the observations is described here. The two hot cores W3(H<sub>2</sub>O) and W3(OH) were observed in 2021 using the IRAM/NOEMA interferometer<sup>1</sup> in the C and D configurations with frequency coverage from 127.823 - 135.311 GHz and 143.116 - 150.666 GHz across the two receiver sidebands. Within the two sidebands, 28 high-resolution spectral windows were selected with channel spacings of 62.5 kHz to better identify and image molecular lines. The data sets were then reduced using the GILDAS packages CLIC and MAPPING<sup>2</sup>, resulting in a synthesized beam of  $\sim 1.87'' \times 1.34''$  (PA =  $-9.3^\circ$ ) in the lower sideband and  $\sim 1.69'' \times 1.22''$  (PA =  $-7.9^\circ$ ) in the upper sideband. Figure 1 in Thompson et al. (2023) shows the imaged continuum at 132 GHz. At this frequency, the continuum emission from W3(OH) consists mostly of free-free emission, while that of W3(H<sub>2</sub>O) is due to dust (Wilner et al. 1995; Wyrowski et al. 1997, 1999; Stecklum et al. 2002).

The spectral fitting procedure described in this work utilizes the Global Optimization and Broadband Analysis Software for Interstellar Chemistry (GOBASIC) in a manner similar to that presented in previous works (Widicus Weaver et al. 2017; Zou & Widicus Weaver 2017; Wright et al. 2022; Thompson et al. 2023). Specifics on GOBASIC operation are described in Rad et al. (2016), with additional modifications described in Thompson et al. (2023). Furthermore, the fitting proce-

cedure used in this work directly parallels the procedure described in-depth in Thompson et al. (2023). However, a very brief discussion of GOBASIC is provided here. Rather than fitting individual lines in the spectrum for each molecule, GOBASIC performs a broadband analysis of molecular spectra by comparing the observational spectra to molecular catalog information provided by the Cologne Database for Molecular Spectroscopy and the Jet Propulsion Laboratory (JPL) Spectral Line Catalog (Müller et al. 2001, 2005; Pickett et al. 1998). By assuming local thermodynamic equilibrium (LTE) and Gaussian line shapes, GOBASIC utilizes the Pattern Search Algorithm to iteratively vary the physical parameters until the simulation matches the observations and a global minimum fit is found. GOBASIC is useful in that it can fit multiple molecules and physical components simultaneously, allowing for a thorough and comprehensive analysis of the spectra. Through this analysis, values for column density in cm<sup>-2</sup>, spectral line full width half maximum ( $\Delta v$ ) in km s<sup>-1</sup>, rotational temperature in K, and velocity shift relative to the  $v_{lsr}$  in km s<sup>-1</sup> can be derived. In this work, molecular spectra were first extracted at each pixel from the data cubes. Each pixel is smaller than the synthesized beam at  $\sim 0.23'' \times 0.23''$ . They were then analyzed using GOBASIC to obtain parameter values for the  $v = 0$  states of SO<sub>2</sub>, CH<sub>3</sub>CN, CH<sub>3</sub>CH<sub>2</sub>CN, and CH<sub>3</sub>OCH<sub>3</sub>, the  $v_t = 0-2$  state of CH<sub>3</sub>OH, and the  $v_t = 0-1$  state for HCOOCH<sub>3</sub>. These components account for the majority of detected spectral lines in the observed frequency ranges. The spectrum extracted at the pixel corresponding to the peak of the continuum flux in each core can be seen in Thompson et al. (2023).

## 3. PARAMETER MAPS

As demonstrated in Thompson et al. (2023), the NOEMA spectral cubes can be used to create parameter maps for the detected molecules that have a sufficient number of lines to enable robust spectral fitting. General specifics on the process of creating these maps are described in Thompson et al. (2023), though the current work includes slight modifications. From the spectra, fits of all six molecules were conducted using GOBASIC to derive values for column density, temperature, and velocity shift relative to the  $v_{lsr}$ . Maps were then constructed using this information via the methods described in Thompson et al. (2023). Previously, only temperature and column density maps were created for CH<sub>3</sub>OH by analyzing it as a singular molecular component with GOBASIC. Here, all six molecules were fit simultaneously using GOBASIC. From this, updated temperature, column density, and velocity shift

<sup>1</sup> IRAM is supported by INSU/CNRS (France), MPG (Germany), and IGN (Spain).

<sup>2</sup> <http://www.iram.fr/IRAMFR/GILDAS>

maps were determined for  $\text{CH}_3\text{OH}$ , along with new maps for  $\text{CH}_3\text{CH}_2\text{CN}$ ,  $\text{CH}_3\text{CN}$ ,  $\text{CH}_3\text{OCH}_3$ ,  $\text{HCOOCH}_3$ , and  $\text{SO}_2$ . The temperature, column density, and velocity shift maps for each molecule are shown in Figures 1, 2, and 3, respectively. Uncertainty maps for each parameter can be found in Appendix A. As  $\text{CH}_3\text{OH}$ ,  $\text{CH}_3\text{CN}$ ,  $\text{CH}_3\text{OCH}_3$ , and  $\text{HCOOCH}_3$  have many strong spectral lines in the observed frequency range, they are good choices for this mapping process. Likewise, these molecules have been used in the past to study this source (Ahmadi et al. 2018; Qin et al. 2015; Chen et al. 2006; Widicus Weaver et al. 2017; Thompson et al. 2023). In addition,  $\text{CH}_3\text{CH}_2\text{CN}$  was included in the current analysis because it was previously well-fit in  $\text{W3(H}_2\text{O)}$  (Widicus Weaver et al. 2017; Thompson et al. 2023). While  $\text{CH}_3\text{CH}_2\text{CN}$  was not previously well-fit in  $\text{W3(OH)}$ , the results presented here show that some pixels near the southern side of the core can be fit with accurate values.  $\text{SO}_2$  was also included in this analysis because it was well-fit across both cores and is prominent in ultra-compact HII regions (Minh et al. 2010). For both the temperature and column density maps, there is a slight offset between the peak values and the peak of the continuum emission. This is further discussed in Section 4.1.

### 3.1. $\text{CH}_3\text{CH}_2\text{CN}$

$\text{CH}_3\text{CH}_2\text{CN}$  proved difficult to fit in  $\text{W3(OH)}$  due to severe line blending from unidentified molecules in the spectra as described by Thompson et al. (2023). Nevertheless, spectra from a small portion of the core had a sufficient number of unblended lines to enable determination of parameters. The maps show both a higher temperature and a higher column density for  $\text{CH}_3\text{CH}_2\text{CN}$  in  $\text{W3(H}_2\text{O)}$  as compared to  $\text{W3(OH)}$ .  $\text{CH}_3\text{CH}_2\text{CN}$  in  $\text{W3(H}_2\text{O)}$  peaks around 130 K and  $4.0 \times 10^{15} \text{ cm}^{-2}$  with a gradual increase in velocity shift from around  $-4.0 \text{ km s}^{-1}$  to  $1.0 \text{ km s}^{-1}$  east to west. The few well-fit pixels in  $\text{W3(OH)}$  peak at lower values around 100 K and  $9.0 \times 10^{14} \text{ cm}^{-2}$  with a gradual increase in velocity shift from around  $-2.0 \text{ km s}^{-1}$  to  $3.0 \text{ km s}^{-1}$  east to west. This analysis not only confirms the presence of  $\text{CH}_3\text{CH}_2\text{CN}$  in  $\text{W3(OH)}$ , but also provides the first quantitative analysis of the molecule in this region.

### 3.2. $\text{CH}_3\text{CN}$

Similar to the procedures followed by Ahmadi et al. (2018) and Thompson et al. (2023), precautions were taken when fitting parameters for  $\text{CH}_3\text{CN}$ . For each spectra across both cores, the  $8(7) - 7(7)$ ,  $8(6) - 7(6)$ , and  $8(5) - 7(5)$  transitions were excluded from the fit because they were severely blended with other molecules.

$\text{CH}_3\text{CN}$  shows both a higher temperature and a higher column density in  $\text{W3(H}_2\text{O)}$ . We find that  $\text{CH}_3\text{CN}$  peaks in  $\text{W3(H}_2\text{O)}$  around 190 K and  $1.0 \times 10^{16} \text{ cm}^{-2}$ , with a gradual increase in velocity shift from around  $-4.0 \text{ km s}^{-1}$  to  $1.0 \text{ km s}^{-1}$  east to west.  $\text{CH}_3\text{CN}$  in  $\text{W3(OH)}$  peaks around 100 K and  $3.0 \times 10^{15} \text{ cm}^{-2}$  with a gradual increase in velocity shift from around  $1.5 \text{ km s}^{-1}$  to  $3.5 \text{ km s}^{-1}$  north to south before decreasing down to  $-2.0 \text{ km s}^{-1}$  at the southern-most region.

### 3.3. $\text{CH}_3\text{OCH}_3$

$\text{CH}_3\text{OCH}_3$  shows a higher temperature in  $\text{W3(OH)}$ , yet a higher column density in  $\text{W3(H}_2\text{O)}$ . We find that  $\text{CH}_3\text{OCH}_3$  peaks in  $\text{W3(H}_2\text{O)}$  around 120 K and  $4.8 \times 10^{17} \text{ cm}^{-2}$ , with a gradual increase in velocity shift from around  $-4.0 \text{ km s}^{-1}$  to  $0.5 \text{ km s}^{-1}$  east to west.  $\text{CH}_3\text{OCH}_3$  in  $\text{W3(OH)}$  peaks around 150 K and  $6.0 \times 10^{16} \text{ cm}^{-2}$ , with a gradual decrease in velocity shift from around  $4.0 \text{ km s}^{-1}$  to  $1.0 \text{ km s}^{-1}$  east to west. The temperature map for  $\text{CH}_3\text{OCH}_3$  presents an intriguing question: what is causing the weak spectra for  $\text{CH}_3\text{OCH}_3$  on the southeast side of  $\text{W3(OH)}$  as compared to the rest of the core? In the column density and velocity shift maps, this region is characterized by a stark decrease in value compared to those derived from the surrounding spectra. Ahmadi et al. (2018) sees two intensity peaks in  $\text{W3(OH)}$  in the integrated intensity map for  $\text{CH}_3\text{CN}$  around  $\sim \delta(\text{J2000}) = 61^\circ 52' 25''.5$  and  $\sim \delta(\text{J2000}) = 61^\circ 52' 23''$ , with the latter peak being consistent with the area of interest in the current work. This dramatic change in physical parameters as compared to the rest of the core could be indicative of a distinct physical component in the core structure. Further analysis with higher spatial resolution could be beneficial to solving this mystery.

### 3.4. $\text{CH}_3\text{OH}$

As mentioned above, new  $\text{CH}_3\text{OH}$  maps were created from fits utilizing multiple molecular components. In these maps,  $\text{CH}_3\text{OH}$  shows a higher temperature in  $\text{W3(OH)}$  and similar column densities in both cores.  $\text{CH}_3\text{OH}$  peaks in  $\text{W3(H}_2\text{O)}$  around 200 K and  $2.7 \times 10^{17} \text{ cm}^{-2}$ , with a gradual increase in velocity shift from around  $-4.0 \text{ km s}^{-1}$  to  $0.0 \text{ km s}^{-1}$  east to west.  $\text{CH}_3\text{OH}$  peaks in  $\text{W3(OH)}$  around 220 K and  $2.7 \times 10^{17} \text{ cm}^{-2}$  with a gradual increase in velocity shift from around  $1.0 \text{ km s}^{-1}$  to  $3.5 \text{ km s}^{-1}$  north to south. The results for temperature and column density are consistent with the results presented by Thompson et al. (2023).

### 3.5. $\text{HCOOCH}_3$

$\text{HCOOCH}_3$  shows both a higher temperature and a higher column density in  $\text{W3(H}_2\text{O)}$ .  $\text{HCOOCH}_3$  peaks

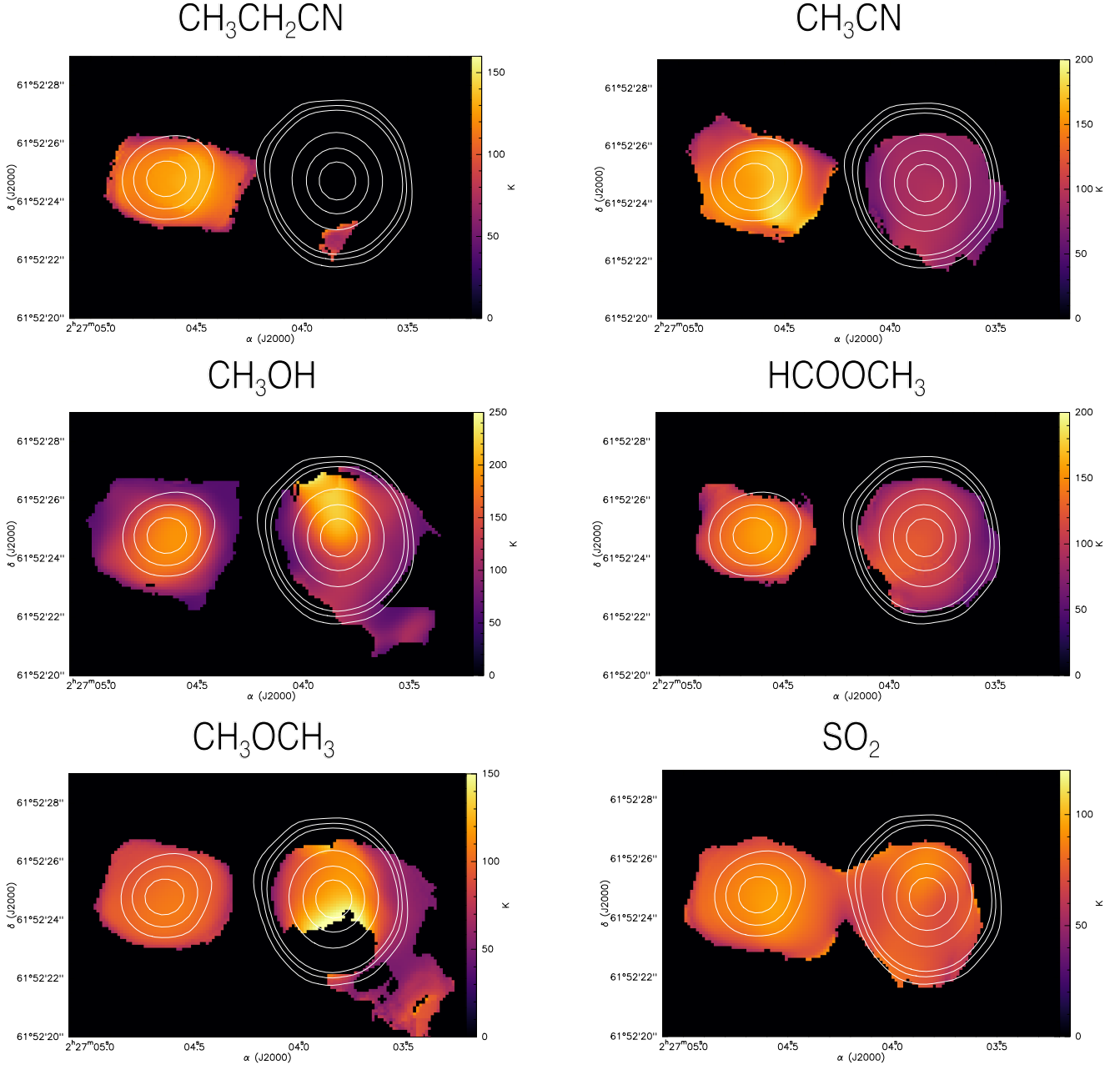


**Figure 1.** Temperature maps for the six molecules obtained by fitting the spectrum at each individual pixel. All six molecules were fit simultaneously using GOBASIC. The white contour levels correspond to the continuum levels in Thompson et al. (2023) at 12, 18, 25, 100, 200, 300 times  $\sigma$  ( $\sigma = 6.481 \text{ mJy beam}^{-1}$ ).

in W3(H<sub>2</sub>O) around 150 K and  $8.0 \times 10^{16} \text{ cm}^{-2}$ , with a gradual increase in velocity shift from around  $-4.0 \text{ km s}^{-1}$  to  $1.0 \text{ km s}^{-1}$  east to west. HCOOCH<sub>3</sub> peaks in W3(OH) around 120 K and  $3.0 \times 10^{16} \text{ cm}^{-2}$ , with a gradual increase in velocity shift from around  $2.0 \text{ km s}^{-1}$  to  $4.0 \text{ km s}^{-1}$  north to south. Interestingly, the column density and velocity shift maps for HCOOCH<sub>3</sub> seem to be affected by a similar phenomenon as the maps for

CH<sub>3</sub>OCH<sub>3</sub>, although to a lesser degree. The decrease in column density in this area of W3(OH) is small, and the velocity shift is poorly determined in a small region on the southwest side.

### 3.6. SO<sub>2</sub>

SO<sub>2</sub> shows similar temperatures in both cores and a higher column density in W3(H<sub>2</sub>O). SO<sub>2</sub> in W3(H<sub>2</sub>O)

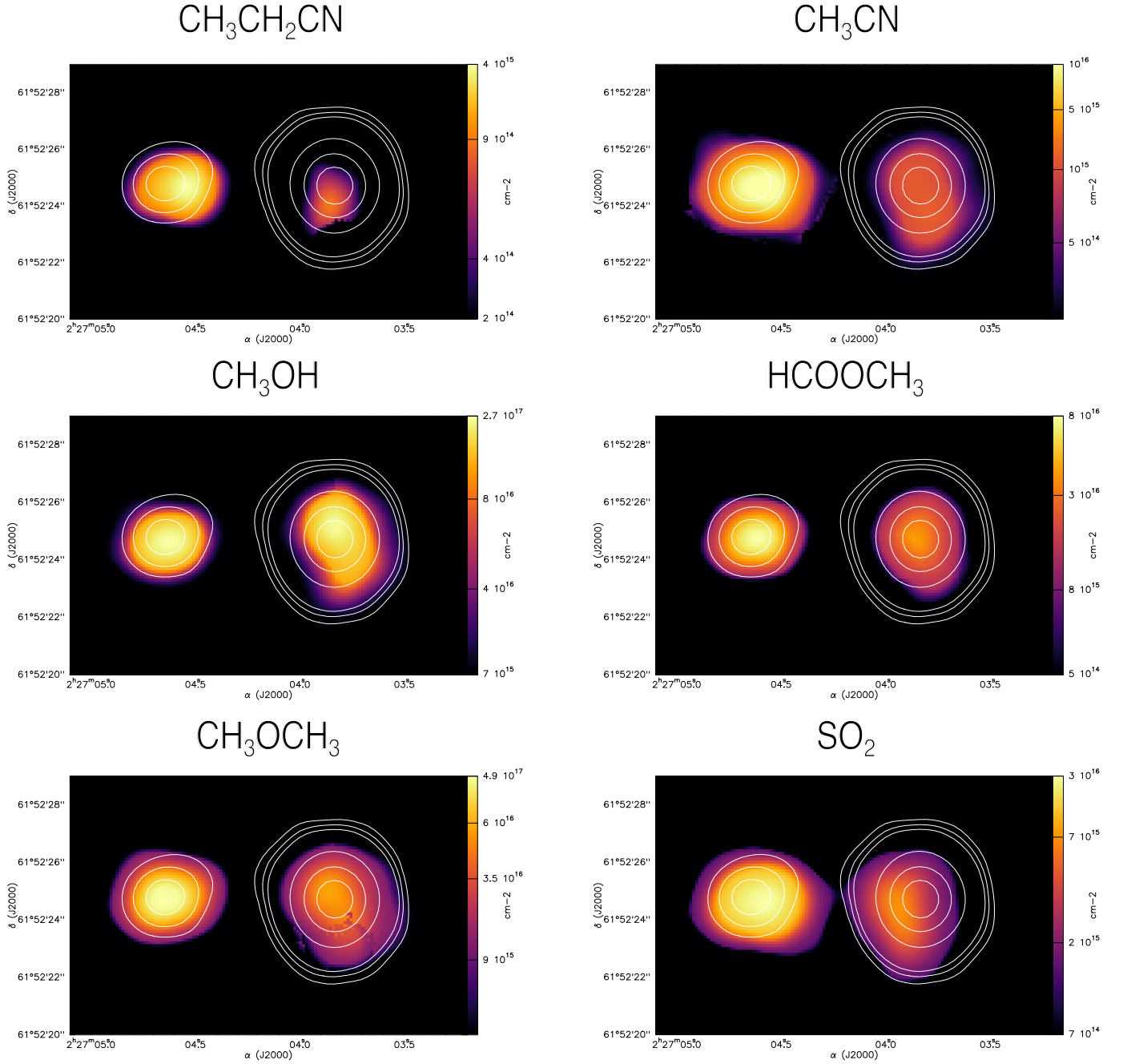


**Figure 2.** Column density maps for the six molecules obtained by fitting the spectrum at each individual pixel. All six molecules were fit simultaneously using GOBASIC. The white contour levels correspond to the continuum levels in Thompson et al. (2023) at 12, 18, 25, 100, 200, 300 times  $\sigma$  ( $\sigma = 6.481 \text{ mJy beam}^{-1}$ ).

peaks around 100 K and  $3.0 \times 10^{16} \text{ cm}^{-2}$ , and in W3(OH) peaks around 100 K and  $7.0 \times 10^{15} \text{ cm}^{-2}$ . The velocity shift map for  $\text{SO}_2$  is unlike that for any of the other molecules in this analysis. From east to west encompassing both cores, the velocity first increases from around  $-4.0 \text{ km s}^{-1}$  to  $1.0 \text{ km s}^{-1}$ , proceeds to decrease to  $-1.0 \text{ km s}^{-1}$ , before finally increasing up to  $4.0 \text{ km s}^{-1}$ . The southwest region of W3( $\text{H}_2\text{O}$ ) and the southwest region of W3(OH) tend to the extreme with values

around  $4.0 \text{ km s}^{-1}$  and  $-4 \text{ km s}^{-1}$ , respectively. All of the  $\text{SO}_2$  maps show a lack of molecular emission from the west side of W3(OH). This is consistent with the integrated intensity map shown in Thompson et al. (2023).

Sulfur chemistry is widely used as an indicator of age in hot cores (Helmich et al. 1994; Charnley 1997; Hatchell et al. 1998; Wakelam et al. 2004). Previously created models for young hot cores predict  $\text{SO}_2$  to first increase, then decrease in abundance as the core



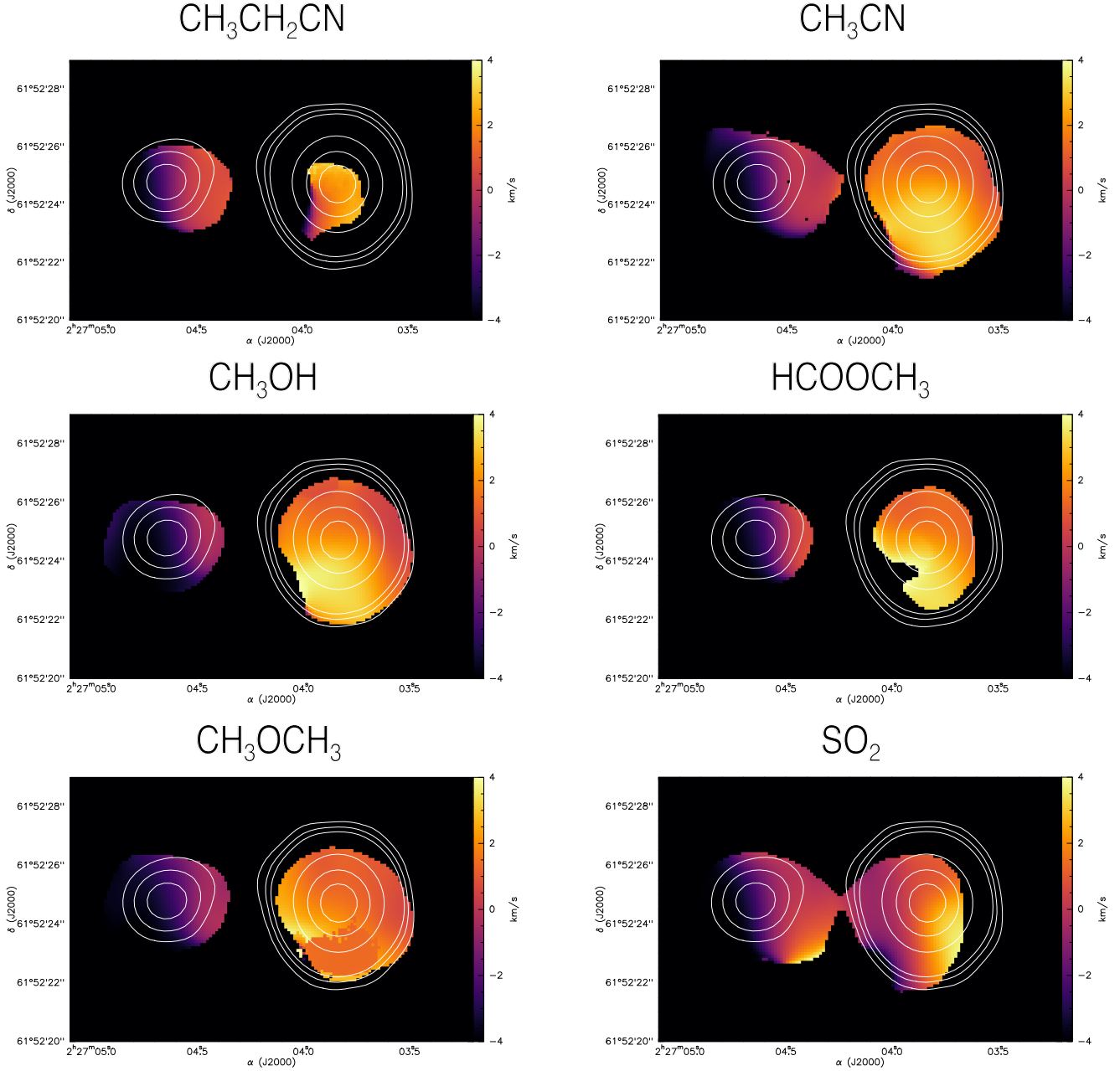


**Figure 3.** Velocity shift maps for the six molecules obtained by fitting the spectrum at each individual pixel. All six molecules were fit simultaneously using GOBASIC. The white contour levels correspond to the continuum levels in Thompson et al. (2023) at 12, 18, 25, 100, 200, 300 times  $\sigma$  ( $\sigma = 6.481 \text{ mJy beam}^{-1}$ ).

progresses in its evolutionary cycle (Millar et al. 1997; Hatchell et al. 1998). This eventual decrease in abundance is evident in the column density map for  $\text{SO}_2$  with peak values for W3( $\text{H}_2\text{O}$ ) being higher than those for W3(OH), as W3(OH) is at a later evolutionary stage than W3( $\text{H}_2\text{O}$ ).  $\text{SO}_2$  is the only molecule shown with a temperature map that does not have significant differences in temperature between W3( $\text{H}_2\text{O}$ ) and W3(OH),

despite the differences in column density between the cores.

#### 4. DISCUSSION

The parameter maps for the W3 cores that are presented above reveal new physical insight into the chemistry, structure, and kinematics of these sources. These findings are discussed below.

#### 4.1. Shift in Peak Emission Position in W3(H<sub>2</sub>O)

The temperature and density peaks for CH<sub>3</sub>CH<sub>2</sub>CN, CH<sub>3</sub>CN, HCOOCH<sub>3</sub>, and SO<sub>2</sub> in W3(H<sub>2</sub>O) are slightly offset to the west from the peak of the continuum emission. This can be attributed to the presence of two embedded protostars, named W3(H<sub>2</sub>O) E and W3(H<sub>2</sub>O) W, within the core (Wyrowski et al. 1999; Ahmadi et al. 2018). W3(H<sub>2</sub>O) E is located at  $\alpha(\text{J2000}) = 02^{\text{h}}27^{\text{m}}04.73^{\text{s}}$ ,  $\delta(\text{J2000}) = 61^{\circ}52'24''.66$  and W3(H<sub>2</sub>O) W at  $\alpha(\text{J2000}) = 02^{\text{h}}27^{\text{m}}04.57^{\text{s}}$ ,  $\delta(\text{J2000}) = 61^{\circ}52'24''.59$  (Ahmadi et al. 2018). Marked positions of the two protostars can be seen in Ahmadi et al. (2018). The maps described in Section 3 show that in W3(H<sub>2</sub>O), the molecular emission traces W3(H<sub>2</sub>O) W while the continuum emission traces W3(H<sub>2</sub>O) E. This is consistent with the findings of Ahmadi et al. (2018) for dense gas tracers such as CH<sub>3</sub>CN and is seen in their integrated intensity maps.

#### 4.2. Comparing Column Density and Temperature Maps

The temperature and column density maps of the complex organic molecules (COMs) reveal that there is not a single value of temperature that can describe the detected molecules in a given core. Temperatures of COMs in both cores range from  $\sim 50$  K to more than 200 K. Likewise, as is expected, column densities vary greatly. However, it appears that the COMs follow similar trends in terms of source kinematics. All COMs display similar velocity shifts. In W3(H<sub>2</sub>O), the velocity shift increases moving east to west. This is similar to the velocity gradient seen in Ahmadi et al. (2018) and provides further evidence for the division of W3(H<sub>2</sub>O) into the two protostars W3(H<sub>2</sub>O) W and W3(H<sub>2</sub>O) E. In W3(OH), apart from the aforementioned southern region of CH<sub>3</sub>OCH<sub>3</sub>, velocity shift increases moving north to south. This seems to be tracing the movement of the non-ionized molecular gas (Keto et al. 1995; Wilner et al. 1999; Ahmadi et al. 2018).

In order to directly compare the temperature and column density values between different molecules, ratio maps between CH<sub>3</sub>OH and the other molecules were created. CH<sub>3</sub>OH was chosen to be the comparison molecule as it had the highest peak temperature and column density values out of the six well-fit molecules. The temperature and column density ratio maps are shown in Figures 4 and 5.

The temperature ratio maps show that CH<sub>3</sub>OH has a much steeper decrease in temperature values moving outward from the center of each core as compared to other molecules. The derived temperature values for CH<sub>3</sub>OH are smaller than those of any of the other

molecules on the edges of the cores in some locations. In the region of the cores near the continuum emission peak, CH<sub>3</sub>OH is warmer than other molecules by up to a factor of two. The values for CH<sub>3</sub>CN in W3(OH) are the outlier to this trend, with the calculated ratio staying within the range of 0.5 - 1.0.

It is interesting to note the difference between the temperature ratio map of CH<sub>3</sub>OCH<sub>3</sub>/CH<sub>3</sub>OH and that of HCOOCH<sub>3</sub>/CH<sub>3</sub>OH. The CH<sub>3</sub>OCH<sub>3</sub>/CH<sub>3</sub>OH temperature ratio map has values  $\sim 0.4$  in the center of W3(H<sub>2</sub>O), and the HCOOCH<sub>3</sub>/CH<sub>3</sub>OH temperature ratio map has values  $\sim 0.75$  towards the center of W3(H<sub>2</sub>O). Similarly to that observed in the parameter maps, the region on the south side of W3(OH) that is showing unusual behavior is also evident in the temperature ratio maps for both CH<sub>3</sub>OCH<sub>3</sub> and HCOOCH<sub>3</sub>. In addition, this region is now apparent in the temperature ratio maps for CH<sub>3</sub>CN and SO<sub>2</sub>, albeit much less significant in these cases.

The column density ratio maps show a much more consistent ratio in both cores across all molecules than do the temperature maps, with most column density ratios peaking around 0.5. In W3(H<sub>2</sub>O), the column density ratios tend to peak on the west side of the core, offset from the continuum peak. In W3(OH), column density ratios tend to peak on the east side of the core, again offset from the continuum peak. CH<sub>3</sub>OCH<sub>3</sub> has the highest column density ratio to CH<sub>3</sub>OH out of all of the molecules, peaking at over 1.0 on the edge of W3(H<sub>2</sub>O).

In W3(H<sub>2</sub>O), both CH<sub>3</sub>OCH<sub>3</sub> and HCOOCH<sub>3</sub> have a ratio that is lower towards the center of the core and higher towards the outside of the core. Because optical depths are low for both molecules, this result is not due to any radiative transfer effect. These molecules are commonly thought of as tracers of grain surface chemistry, forming from the photolysis of CH<sub>3</sub>OH on icy grains (Garrod et al. 2008; Laas et al. 2011). CH<sub>3</sub>OCH<sub>3</sub> and HCOOCH<sub>3</sub> would therefore be expected to have temperature and density profiles similar to that of CH<sub>3</sub>OH. However, the column density ratio maps show this is not the case. The column density ratio map of CH<sub>3</sub>OCH<sub>3</sub>/CH<sub>3</sub>OH yields higher values outside of the continuum contours, indicating a higher column density of CH<sub>3</sub>OCH<sub>3</sub> outside of the continuum, where there is less CH<sub>3</sub>OH. It is not clear if this is an artifact of the spectral line fits for these molecules in the region outside of the continuum, or if there actually is a higher abundance of CH<sub>3</sub>OCH<sub>3</sub> and HCOOCH<sub>3</sub> in this region. When looking at the individual spectra in this region, there are no obvious indicators of artifacts. Furthermore, the signal-to-noise ratio is consistent with that

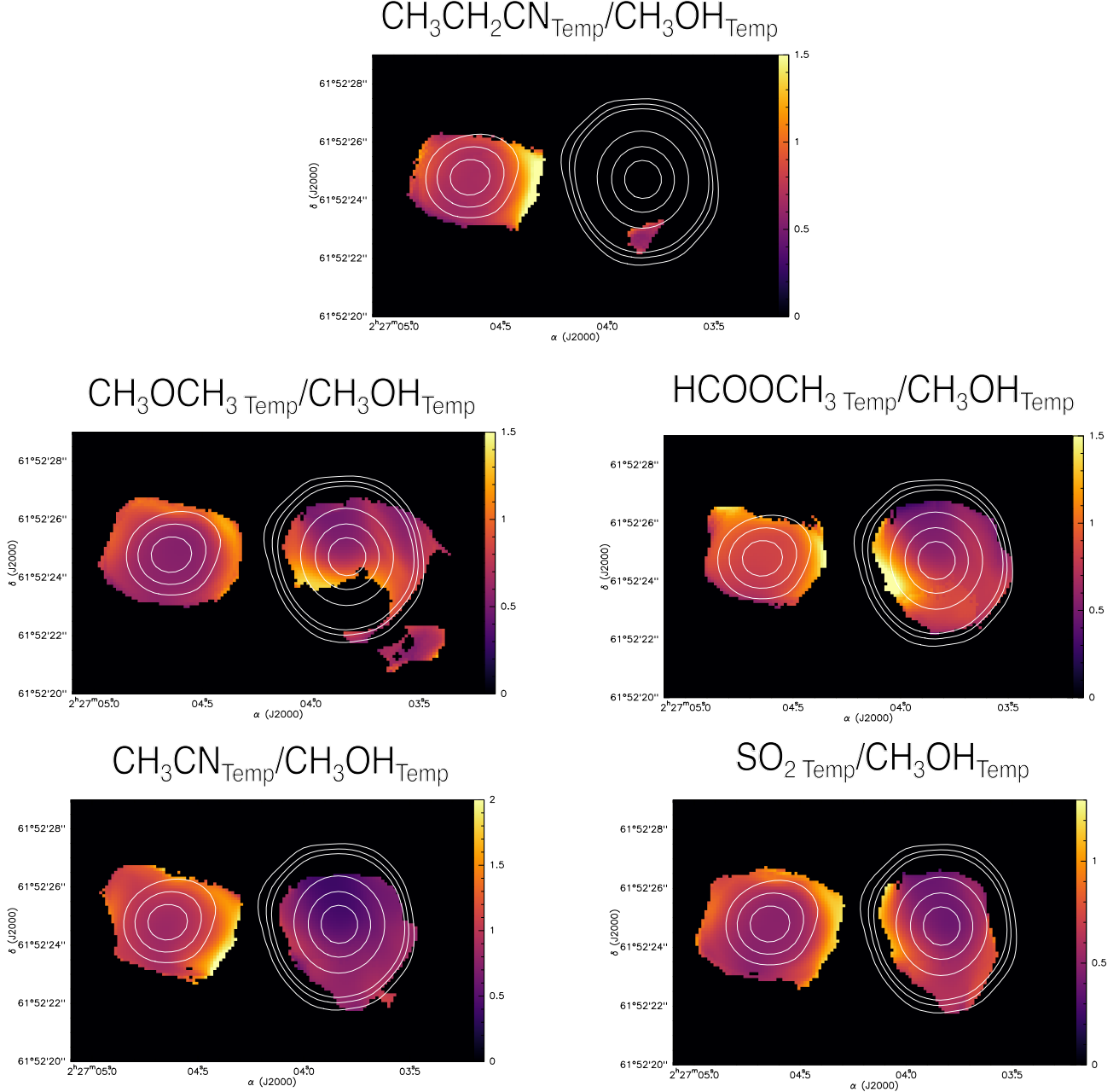


**Figure 4.** Temperature ratio maps comparing each molecule to  $\text{CH}_3\text{OH}$ . For each molecule, the derived temperature value at each pixel was divided by the corresponding  $\text{CH}_3\text{OH}$  temperature value. The white contour levels correspond to the continuum levels in [Thompson et al. \(2023\)](#) at 12, 18, 25, 100, 200, 300 times  $\sigma$  ( $\sigma = 6.481 \text{ mJy beam}^{-1}$ ).

in spectra from other areas in the core. If  $\text{CH}_3\text{OCH}_3$  is forming from photolysis of  $\text{CH}_3\text{OH}$  in the ice, one would expect the density maps of  $\text{CH}_3\text{OCH}_3$  and  $\text{HCOOCH}_3$  to trace the same spatial area as  $\text{CH}_3\text{OH}$ . The region of unusual structure once again appears in the maps for  $\text{CH}_3\text{OCH}_3$ ,  $\text{HCOOCH}_3$ , and  $\text{CH}_3\text{CN}$ .

To further analyze the relationship in column densities and temperatures between each pair of molecules,

we follow a similar technique used in [Law et al. \(2021\)](#) to create Figures 6 and 7. In Figure 6, we compare the calculated column density values at each individual pixel. Every plot has a clear separation into a component for  $\text{W3}(\text{H}_2\text{O})$  and a component for  $\text{W3}(\text{OH})$ . Furthermore, most pairs of molecules have a direct correlation in column densities. The outlier to this trend lies in the comparison of molecules to  $\text{CH}_3\text{CH}_2\text{CN}$  in



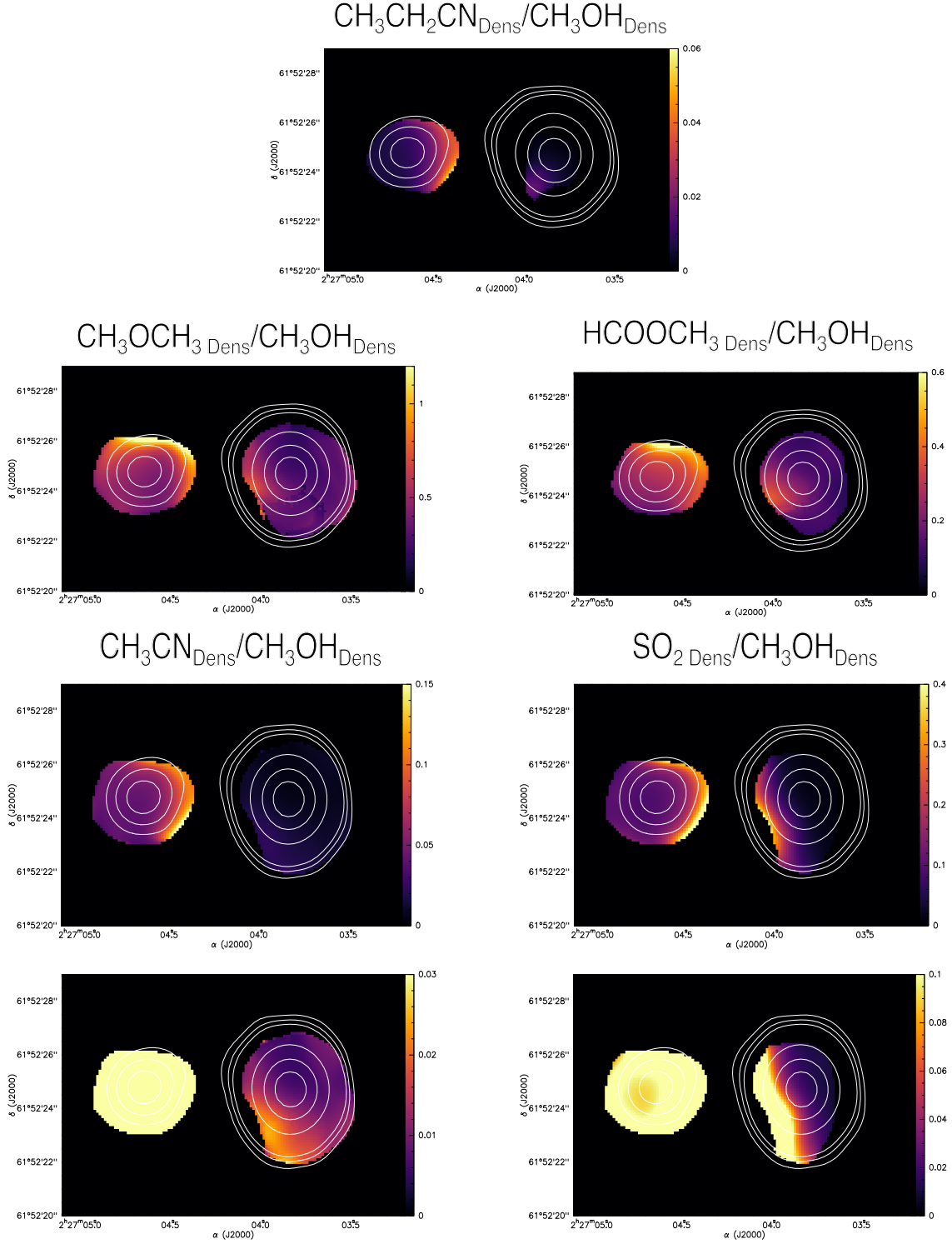


**Figure 5.** Column density ratio maps comparing each molecule to  $\text{CH}_3\text{OH}$ . For each molecule, the derived column density value at each pixel was divided by the corresponding  $\text{CH}_3\text{OH}$  column density value. The white contour levels correspond to the continuum levels in Thompson et al. (2023) at 12, 18, 25, 100, 200, 300 times  $\sigma$  ( $\sigma = 6.481 \text{ mJy beam}^{-1}$ ). The  $\text{CH}_3\text{CN}$  and  $\text{SO}_2$  ratio maps are shown using two maps to exhibit the vast difference between cores.

W3(OH) due to the low signal-to-noise spectra in many

regions of the core. However, the  $\text{CH}_3\text{CH}_2\text{CN}$  values

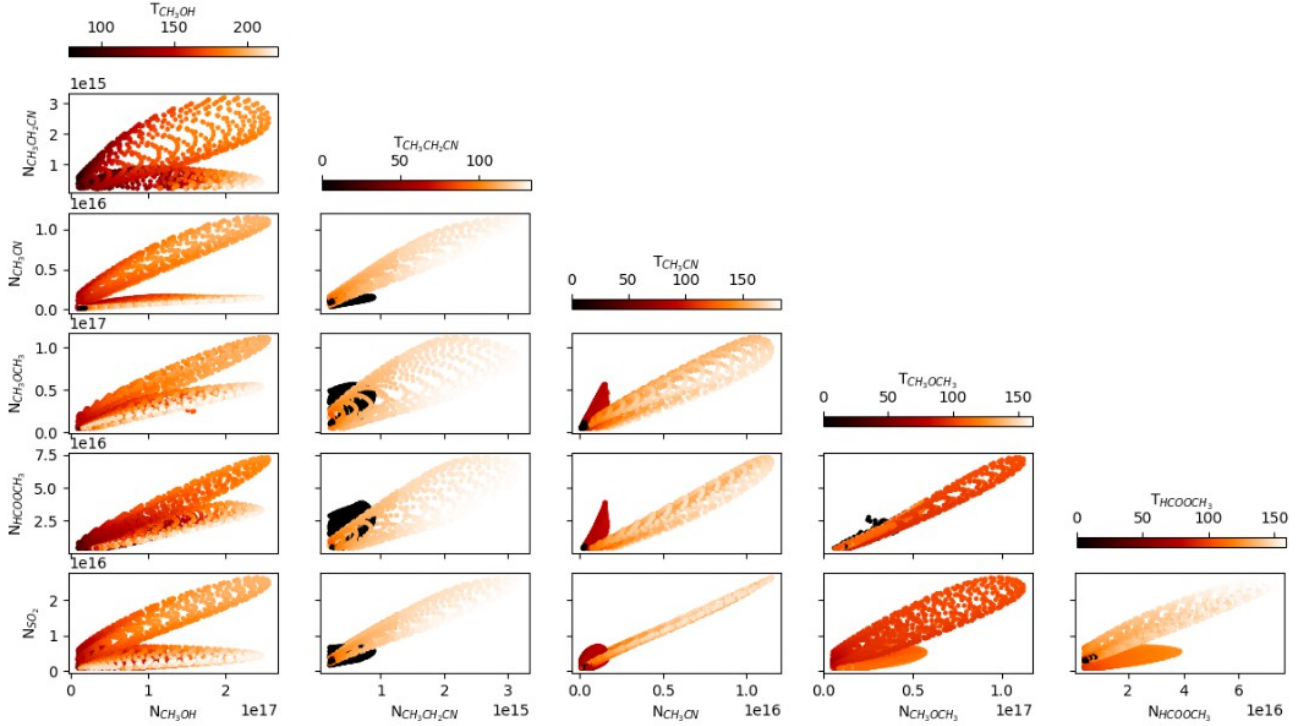


**Figure 6.** Plots comparing column densities in  $\text{cm}^{-2}$  between two molecules. The color bar denotes temperature in K of the molecule on the x-axis. Black data points denote where the fits for column density do not overlap with the fits for temperature (most evident in the pixels in W3(OH) for  $\text{CH}_3\text{CH}_2\text{CN}$ ). It should be noted that since the pixel size is smaller than the synthesized beam, these plots are over-sampled. However, due to the asymmetric nature of the two cores, re-binning the data to account for the size of the synthesized beam would introduce additional averaging errors.

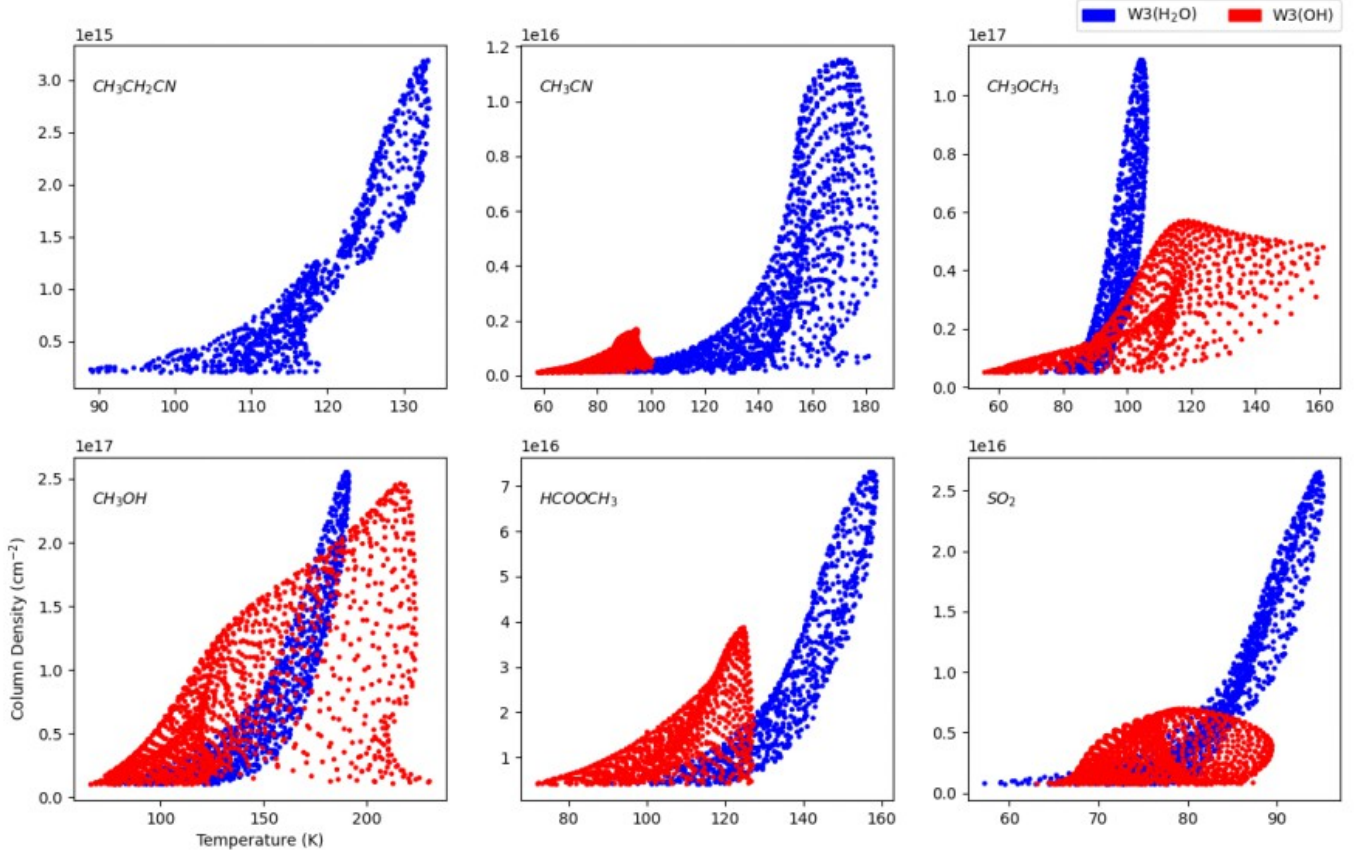
in W3(OH) correlate the best with those of  $\text{CH}_3\text{CN}$ , as a secondary component is seemingly beginning to form similar to that in the comparisons of other molecules. Further analysis of  $\text{CH}_3\text{CH}_2\text{CN}$  in W3(OH) is needed to confirm this.  $\text{CH}_3\text{OH}$ ,  $\text{CH}_3\text{OCH}_3$ , and  $\text{HCOOCH}_3$  all exhibit similar spatial correlations in both cores in agreement with previous studies of these organics in star-forming regions (Bisschop et al. 2007; Widicus Weaver et al. 2017; Law et al. 2021; Thompson et al. 2023). The  $\text{CH}_3\text{CN}$  plots show interesting results similar to those described in Law et al. (2021). While  $\text{CH}_3\text{CN}$  spatially correlates well with every molecule in W3( $\text{H}_2\text{O}$ ), it seems to only correlate well with  $\text{CH}_3\text{OH}$  in W3(OH). This is likely due to both molecules being related to total gas density as opposed to any relation in chemical formation pathways (Garrod & Herbst 2006; Garrod et al. 2008; Law et al. 2021).

Figure 7 compares column density and temperature values for each molecule. For all molecules except  $\text{CH}_3\text{CN}$ , W3( $\text{H}_2\text{O}$ ) exhibits a positive exponential trend. W3(OH) also exhibits a positive trend, however cannot be described with any specific function. This difference can most likely be attributed to the complex nature of the W3(OH). As W3(OH) is an ultra-

compact HII region, most of the gas originates from outside a dusty cocoon surrounding the embedded protostar, while the inner region is ionized (Wynn-Williams et al. 1972; Qin et al. 2015; Thompson et al. 2023). With two different sources of molecular gas in the core, it is difficult to ascertain a specific type of trend in W3(OH).  $\text{CH}_3\text{OH}$ ,  $\text{CH}_3\text{OCH}_3$ , and  $\text{HCOOCH}_3$  are the most obvious examples of this as both molecules show much less compact trends. As stated in Thompson et al. (2023), these molecules are intrinsically linked via formation pathways as both  $\text{CH}_3\text{OCH}_3$  and  $\text{HCOOCH}_3$  can form from chemistry involving methanol photodissociation and the  $\text{CH}_3\text{O}$  radical (Garrod & Herbst 2006; Garrod et al. 2008; Laas et al. 2011; Garrod et al. 2022).

#### 4.3. $\text{CH}_3\text{CN}$ as a Molecular Thermometer

$\text{CH}_3\text{CN}$  is commonly used as a molecular tracer for temperature in hot cores (Loren & de Mundy 1984; Zhang et al. 1998; Ahmadi et al. 2018). It is a symmetric-top molecule with many transitions closely spaced, allowing for direct comparison between the excitation temperatures of similar transitions in different  $K$ -ladders of the rotational spectrum (Loren & de Mundy 1984). In using  $\text{CH}_3\text{CN}$  as a thermometer for hot cores,



**Figure 7.** Plots comparing column density to temperature for each molecule. Derived parameters from spectra located in W3(H<sub>2</sub>O) and W3(OH) are denoted by blue and red, respectively. CH<sub>3</sub>CH<sub>2</sub>CN does not show results for W3(OH) as there were no regions with both well-derived column density and well-derived temperature.

it is important to account for both non-LTE excitation and optical depth effects. As mentioned in Section 3.2, the analysis presented here follows a similar method to Ahmadi et al. (2018) and Thompson et al. (2023), specifically removing the  $K = 5-7$  lines from the analysis. Comparing the temperature map of W3(H<sub>2</sub>O) for CH<sub>3</sub>CN to that presented in Ahmadi et al. (2018), the molecular emission seems to peak in similar locations across the core. However, this work shows peaks at a temperature roughly 100 K lower than the previous work. The results presented here are more consistent with the calculated values for the other five molecules analyzed in this work. Even though similar methods were used in the two maps to account for difficult lines in the spectrum, wildly different results were achieved. One potential reason for the difference in results is that the analysis presented here better accounts for line blending in the CH<sub>3</sub>CN transitions. However, the CH<sub>3</sub>CN transitions presented in Ahmadi et al. (2018) do not seem to suffer from any blending issues apart from the CH<sub>3</sub><sup>13</sup>CN isotopologue, which is accounted for in their fitting. It could also be due to the difference

in rotational level energies, as the analyzed transitions presented here have lower energies than those in Ahmadi et al. (2018).

To counter this problem in future studies of W3(H<sub>2</sub>O) and W3(OH), we propose the use of HCOOCH<sub>3</sub> as the main tracer for temperature in these specific star-forming cores. While HCOOCH<sub>3</sub> has been used as a molecular tracer for temperature in similar sources, it has yet to be used for W3(H<sub>2</sub>O) and W3(OH) (Gorai et al. 2021; Brouillet et al. 2022). HCOOCH<sub>3</sub> is not a symmetric-top molecule like CH<sub>3</sub>CN and as such does not have similar transitions in different  $K$ -ladders for comparison. However, the use of HCOOCH<sub>3</sub> as a tracer removes the need for accounting for optical depth effects. In all spectra across both cores, HCOOCH<sub>3</sub> had no optically-thick transitions. Furthermore, when comparing the temperature maps of all six molecules, the values and emission shapes for CH<sub>3</sub>CN are most similar to those for HCOOCH<sub>3</sub> in each core.

## 5. CONCLUSIONS

We have carried out millimeter-wave observations of the W3(H<sub>2</sub>O) and W3(OH) star-forming regions using the IRAM/NOEMA interferometer. From these observations, a spectrum at each individual pixel was extracted and fit using GOBASIC for the molecules CH<sub>3</sub>OH, CH<sub>3</sub>CH<sub>2</sub>CN, CH<sub>3</sub>CN, CH<sub>3</sub>OCH<sub>3</sub>, HCOOCH<sub>3</sub>, and SO<sub>2</sub>. Rotational temperature, column density, and velocity shift relative to the  $v_{lsr}$  were then determined at each pixel. Physical parameter maps for each of the six molecules were then created. Additionally, ratio maps were created for temperature and column density to compare each molecule to CH<sub>3</sub>OH. Further plots were created to discuss the spatial comparison of these values between molecules.

Temperatures and column densities vary across the six molecules, ranging from 50 K to 200 K and  $4.0 \times 10^{14} \text{ cm}^{-2}$  to  $4.9 \times 10^{17} \text{ cm}^{-2}$ , respectively. As CH<sub>3</sub>CN has consistently proven difficult to accurately fit in studies of the two cores, we suggest HCOOCH<sub>3</sub> as an alternative for tracing temperature in this region. SO<sub>2</sub>, the only inorganic molecule analyzed in this study, revealed the most consistent temperature across both cores, peaking at  $\sim 100$  K in each core. SO<sub>2</sub> also has a lower column density in W3(OH), supporting previous models describing a decrease in the molecule at later stages of star formation. Generally, the results from this study for temperature and column density are consistent with previous analyses of these molecules in this region (Qin et al. 2015; Widicus Weaver et al. 2017; Ahmadi et al. 2018; Thompson et al. 2023). Furthermore, the veloc-

ity shift maps support the claim made in Ahmadi et al. (2018) that W3(H<sub>2</sub>O) is split into the two embedded protostars W3(H<sub>2</sub>O) W and W3(H<sub>2</sub>O) E. This claim is also supported by the shift in molecular peak emission to the west of the continuum peak emission that was observed in the current work.

When comparing the column densities of any pair of molecules, both cores exhibit a direct, positive correlation. While the N- and O-bearing organic species each follow their own similar trends, there is an overlap with CH<sub>3</sub>OH and CH<sub>3</sub>CN due to both being related to total gas density (Garrod & Herbst 2006; Garrod et al. 2008; Law et al. 2021). In W3(H<sub>2</sub>O), each individual molecule apart from CH<sub>3</sub>CN shows a compact, exponential trend when comparing column density and temperature. W3(OH) is more complicated because it is an HII region, but generally shows a positive trend for each molecule.

## 6. ACKNOWLEDGEMENTS

S.L.W.W., M.M.G., and W.E.T. thank the University of Wisconsin-Madison for S.L.W.W.’s startup support and access to NOEMA time that enabled this research. We thank Ka Tat Wong from IRAM for support in setting up the observations and initial data reduction. Part of this research was carried out at the Jet Propulsion Laboratory, California Institute of Technology, under a contract with the National Aeronautics and Space Administration (80NM0018D0004).

*Software:* Astropy (Astropy Collaboration et al. 2013, 2018, 2022)

## APPENDIX

### A. UNCERTAINTY MAPS

This section provides uncertainty values for the physical parameters derived using GOBASIC. For each individual pixel, the derived value of temperature, column density, and velocity shift described in Figures 1, 2, and 3 was divided by the corresponding uncertainty. Figures 8, 9, and 10 plot these fractions spatially on a logarithmic scale. These fractions represent two important physical values. First, they are the inverse of the fractional uncertainty. Second, they are the signal-to-noise ratio at each pixel. The more negative the value in the plot, the higher the fractional uncertainty and the lower the signal-to-noise.

## REFERENCES

- |  |   |
|--|---|
| <p>Ahmadi, A., Beuther, H., Mottram, J. C., et al. 2018, A&amp;A, 618</p> <p>Altwegg, K., Balsiger, H., &amp; Fuselier, S. A. 2019, Annual Review of A&amp;A, 57, 113</p> <p>Astropy Collaboration, Robitaille, T. P., Tollerud, E. J., et al. 2013, A&amp;A, 558, A33</p> | <p>Astropy Collaboration, Price-Whelan, A. M., Sipőcz, B. M., et al. 2018, AJ, 156, 123</p> <p>Astropy Collaboration, Price-Whelan, A. M., Lim, P. L., et al. 2022, ApJ, 935, 167</p> <p>Bisschop, S. E., Jørgensen, J. K., van Dishoeck, E. F., &amp; de Wachter, E. B. M. 2007, A&amp;A, 465, 913</p> |
|--|---|

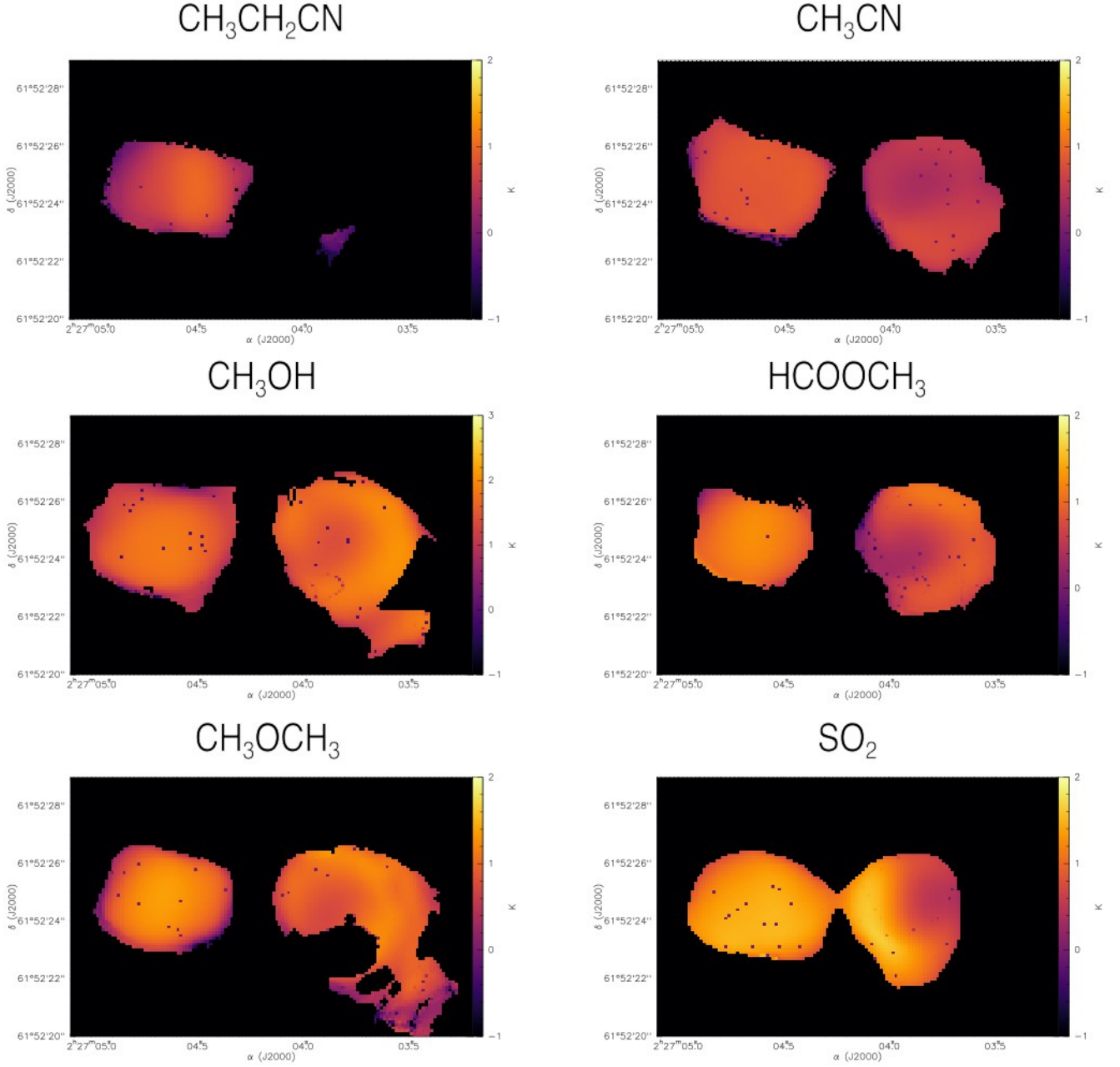


**Figure 8.** Maps describing the uncertainty of temperature values for each molecule.

Blake, G. A., & van Dishoeck, E. F. 1998, Annual Review of A&A, 36, 317

Brouillet, N., Despois, D., Molet, J., et al. 2022, A&A, 665, A140

Charnley, S. B. 1997, ApJ, 481, 396

Chen, H., Welch, W. J., Wilner, D. J., & Sutton, E. C. 2006, ApJ, 639, 975

Chyba, C., & Sagan, C. 1992, Nature, 355, 125

Chyba, C. F., Thomas, P. J., Brookshaw, L., & Sagan, C. 1990, Science, 249, 366

Garrod, R., & Herbst, E. 2006, A&A, 457, 927

Garrod, R., Mihwa, J., Matis, K., Jones, D., & Willis, E. and Herbst, E. 2022, ApJS, 249, 26

Garrod, R., Widicus Weaver, S.L., & Herbst, E. 2008, ApJ, 682, 283

Gorai, P., Das, A., Shimonishi, T., et al. 2021, ApJ, 907, 108



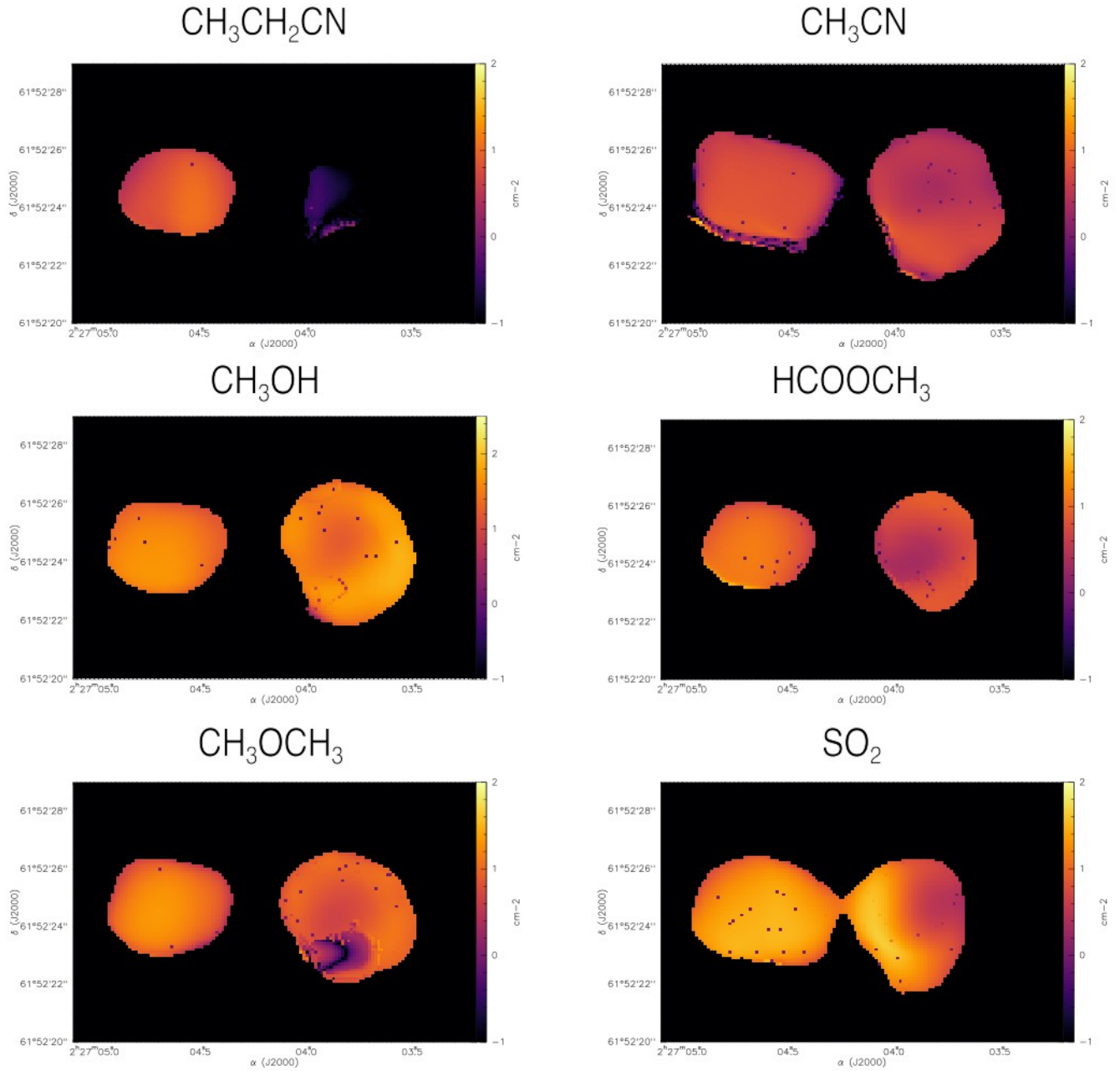


**Figure 9.** Maps describing the uncertainty of column density values for each molecule.

- Hartogh, P., Lis, D. C., Bockelée-Morvan, D., et al. 2011, *Nature*, 478, 218
- Hatchell, J., Thompson, M. A., Millar, T. J., & Macdonald, G. H. 1998, *A&A*, 338, 713
- Helmich, F., Jansen, D., de Graauw, T., Groesbeck, T., & van Dishoeck, E. 1994, *Astronomical Society of the Pacific*, 283, 626
- Helmich, F., & van Dishoeck, E. 1997, *A&AS*, 124
- Herbst, E., & van Dishoeck, E. F. 2009, *Annual Review of A&A*, 47, 427
- Jørgensen, J. K., Favre, C., Bisschop, S. E., et al. 2012, *Astrophysical Journal Letters*, 757
- Jørgensen, J. K., Hogerheijde, M. R., Blake, G. A., et al. 2004, *A&A*, 415, 1021
- Keto, E. R., Welch, W. J., Reid, M. J., & Ho, P. T. P. 1995, *ApJ*, 444, 765

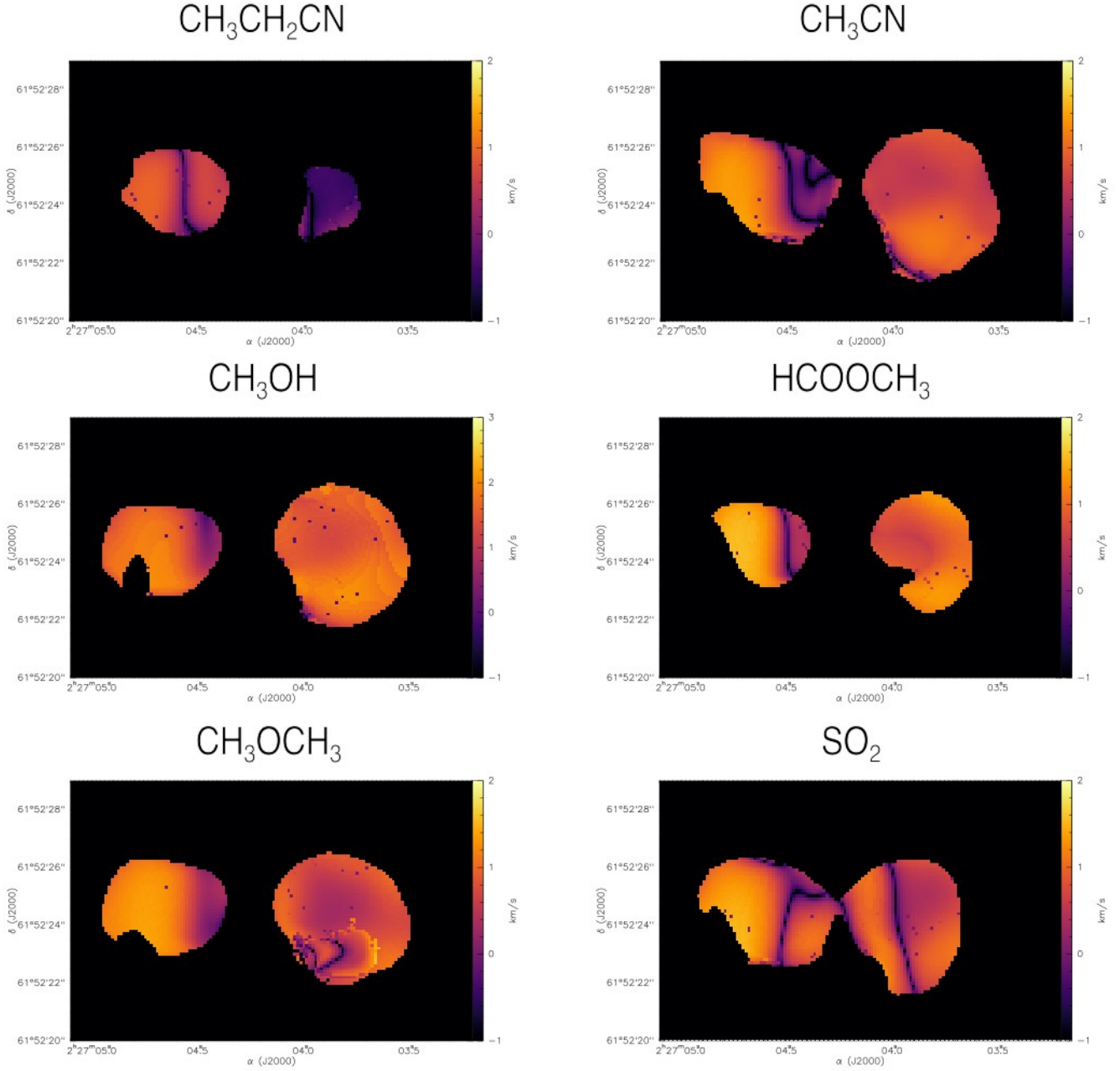


**Figure 10.** Maps describing the uncertainty of velocity shift values for each molecule.

- Laas, J. C., Garrod, Herbst, E., & Weaver, S. L. 2011, *Astrophysical Journal*, 728
- Law, C. J., Zhang, Q., Öberg, K. I., et al. 2021, *ApJ*, 909, 214
- Ligterink, N. F., Ahmadi, A., Luitel, B., et al. 2022, *ACS Earth and Space Chemistry*, 6, 455
- Loren, R. B., & de Mundy, L. G. 1984, *ApJ*, 286, 232
- Millar, T. J., Macdonald, G. H., & Gibb, A. G. 1997, *A&A*, 325, 1163
- Minh, Y. C., Su, Y.-N., Chen, H.-R., et al. 2010, *ApJ*, 723, 1231
- Müller, H., Schlöder, F., Stutzki, J., & Winnewisser, G. 2005, *Journal of Molecular Structure*, 742, 215
- Müller, H., Thorwirth, S., Roth, D. A., & Winnewisser, G. 2001, *A&A*, 370, L49
- Munoz Caro, G. M., Meierhenrich, U., Schutte, W., et al. 2002, *Nature*, 416, 403

- Öberg, K. I., Boogert, A. C., Pontoppidan, K. M., et al. 2011, *Astrophysical Journal*, 740
- Oró, J. 1961, *Nature*, 190, 389
- Pickett, H., Poynter, R., Cohen, E., et al. 1998, *Journal of Quantitative Spectroscopy and Radiative Transfer*, 60, 883
- Qin, S. L., Schilke, P., Wu, J., et al. 2015, *Astrophysical Journal*, 803, 39
- Rad, M. L., Zou, L., Sanders, J. L., & Widicus Weaver, S. L. 2016, *A&A*, 585, 1
- Rivera-Ingraham, A., Martin, P. G., Polychroni, D., et al. 2013, *Astrophysical Journal*, 766
- Rivilla, V. M., Martín-Pintado, J., Jiménez-Serra, I., et al. 2020, *ApJ*, 899, L28
- Stecklum, B., Brandl, B., Henning, T., et al. 2002, *A&A*, 392, 1025
- Thompson, W. E., Giese, M. M., Lis, D. C., & Widicus Weaver, S. L. 2023, *ApJ*, 952, 50
- Tobin, J. J., Hartmann, L., Chiang, H. F., et al. 2011, *Astrophysical Journal*, 740
- Tychoniec, L., van Dishoeck, E. F., Van 't Hoff, M. L., et al. 2021, *A&A*, 655
- van Dishoeck, E. F. 2006, *Proceedings of the National Academy of Sciences of the United States of America*, 103, 12249
- Wakelam, V., Caselli, P., Ceccarelli, C., Herbst, E., & Castets, A. 2004, *A&A*, 422, 159
- Widicus Weaver, S. L., & Friedel, D. N. 2012, *Astrophysical Journal, Supplement Series*, 201
- Widicus Weaver, S. L., Laas, J. C., Zou, L., et al. 2017, *ApJS*, 232, 3
- Wilner, D. J., Reid, M. J., & Menten, K. M. 1999, *ApJ*, 513, 775
- Wilner, D. J., Welch, W. J., & Forster, J. R. 1995, *ApJ*, 449, 73
- Wright, C. J., Smith, R. N., Kroll, J. A., Shipman, S. T., & Widicus Weaver, S. L. 2022, *ACS Earth and Space Chemistry*, 6, 482
- Wynn-Williams, C., Becklin, E., & Neugebauer, G. 1972, *Monthly Notices of the Royal Astronomical Society*, 160, 1
- Wyrowski, F., Hofner, P., Schilke, P., et al. 1997, *A&A*, 320, 17
- Wyrowski, F., Schilke, P., Walmsley, C., & Menten, K. 1999, *ApJ*, 31
- Zhang, Q., Ho, P. T. P., & Ohashi, N. 1998, *ApJ*, 494, 636
- Zou, L., & Widicus Weaver, S. L. 2017, *ApJ*, 849, 139